
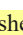


Analysis of the Mechanism of Water Inrush Geohazards in Deep-Buried Tunnels under the Complex Geological Environment of Karst Cave-Fractured Zone

Weishe Zhang¹, Yuyong Jiao^{1*}, Guohua Zhang¹, Xi Zhang¹, Guangzhao Ou¹, Zhiping Lin²

1. Faculty of Engineering, China University of Geosciences, Wuhan 430074, China

2. Fujian Highway Bridge Engineering Co., Ltd., Fuzhou 350000, China

 Weishe Zhang: <https://orcid.org/0000-0003-0394-3031>;  Yuyong Jiao: <https://orcid.org/0000-0001-9081-6932>

ABSTRACT: To study the mechanism and evolution process of water inrush geohazards under the complex geological environment of the karst cave-fractured zone, a large-scale physical three-dimensional (3D) model test was first performed. Then the conceptual model for the evolution process of water inrush geohazards and the simplified theoretical model for the critical hydraulic pressure were both established based on the main characteristics of the water inrush geohazard in the engineering background and that in the model test. A new method was developed for modeling the geological environment of the karst cave-structural plane, and two formulae describing the critical water pressure of water inrush geohazards under two failure models of tensile-shear fracture failure and compression-shear fracture failure were also deduced based on fracture mechanics. The results showed that: (1) the evolution process of the water inrush geohazard can be divided into four stages, which include the initial balance, the propagation of original cracks, the formation of the dominant water inrush channel, and the instability of the waterproof rock mass; (2) the suddenness of water inrush geohazards becomes stronger with the increase of the hydraulic pressure; (3) the calculated critical hydraulic pressure of water inrush geohazards is similar to the measured critical hydraulic pressure in the model test, which validated the accuracies of the theoretical model, and the failure model of water inrush geohazards in this research is compression-shear fracture failure.

KEY WORDS: karst cave, fractured zone, water inrush, mechanism, critical hydraulic pressure, model test, engineering geology.

0 INTRODUCTION

With the development of the social economy and core technologies of deep excavation, tunnel construction has stepped into an era of deep burial and ultralong tunnels, and the subsequent forms of geological disasters have become more diverse. Among them, water inrush geohazard in the complex geological environment has become a key problem facing tunnel construction (Xue et al., 2021; Wang et al., 2020; Simpson and Tatsuoka, 2008; Sun and Wang, 2000). Water inrush is a complex process of multiscale and multifield coupling that is characterized by concealment, complexity, suddenness, and destructiveness (Li et al., 2016). It is difficult to study the catastrophic evolution process in real time when a disaster occurs. Therefore, statistical analysis of engineering

cases, theoretical analysis, and model tests have become common methods used by scholars at home and abroad (Zhang et al., 2017; Farhadian et al., 2016; Moon and Fernandez, 2010; Park et al., 2008; Paul, 2008). Based on the analysis of 221 water inrush cases, Li et al. (2018) divided tunnel water inrush into four typical models (direct exposure, gradual failure, seepage instability, and intermittent failure), which laid a good theoretical foundation for the analysis of the mechanism of water inrush disasters.

Given differences in geological conditions, catastrophe theory, limit equilibrium theory, and fracture mechanics theory can be applied to analyze the disaster mechanism of water inrush in the tunnel. The primary feature of catastrophe theory is that it can describe characteristics such as discreteness, irregularity, and heterogeneity of water inrush disasters in rock systems (Zhu and Li, 2020). Using catastrophe theory, Liang et al. (2016) and Yang and Xiao (2016) developed the cusp catastrophe model and deduced a formula to calculate the critical safe thickness of water inrush in a tunnel. Zhang L W (2021) analyzed the influence of karst shape on the stability and minimum safe thickness of a tunnel using catastrophe theory and strength theory. When catastrophe theory is used to analyze wa-

*Corresponding authors: yujiao@cug.edu.cn;

zhangguohua@cug.edu.cn

© China University of Geosciences (Wuhan) and Springer-Verlag GmbH Germany, Part of Springer Nature 2022

Manuscript received October 20, 2021.

Manuscript accepted January 17, 2022.

ter inrush in the tunnel, the structural mechanical model of the waterproof rock mass should be determined first, but in practical engineering, geological conditions are complex and diverse; thus, it is impossible to establish a suitable structural mechanical model in many cases. Limit equilibrium theory and fracture mechanics theory have been used to analyze the mechanism of water inrush in the tunnel to solve this problem (Xu et al., 2021; Wu et al., 2019; Hu et al., 2018; Nodintsev and Amiletchenko, 2015). Fu et al. (2021) used the limit equilibrium method to analyze the mechanism of water inrush in a tunnel whose axis is perpendicular to the fault and deduced the theoretical calculation formula of the minimum safe thickness. The theory of the slice method was introduced into the analysis of the mechanism of water and mud inrush in filled karst tunnels by Li et al. (2015), providing a new idea for the calculation of water and mud inrush in karst tunnels. Based on the theory of fracture mechanics, Zhang Q et al. (2021) established a mechanical model of water inrush under blasting and excavation conditions for deep-buried tunnels and proposed two types of water inrush: tension-shear damage and compression-shear damage.

The model test is different from the statistical analysis of engineering cases and theoretical derivation. The test can avoid constructing the constitutive relation of complex rock masses when the mechanism research is unclear and explore many problems that cannot be solved by mathematical and mechanical methods (Ameguid et al., 2008). The test provides the basis for a new theory and mathematical model and is widely used to solve the problem of water inrush in tunnels (Su et al., 2020; Liu et al., 2019; Huang et al., 2019; Jiang et al., 2017; Wang and Wang, 2013). Li et al. (2016) analyzed the mechanism of water inrush under fault geological conditions using physical model tests, and results showed that the fault was a key location to prevent and control water inrush in tunnels. Zhao and Zhang (2018) studied the characteristics of water and mud inrush in fractured rock masses through model tests and found that excavation disturbance, high water pressure, and water erosion are key factors that affect water and mud inrush. To investigate the evolution of water inrush in karst tunnels, model tests were performed by Pan et al. (2019), and results indicated that the evolution of water inrush could be categorized into the emergence of water-flowing cracks, the formation of the dominant water channel, and the collapse of the water-proof rock mass. Wang et al. (2021) researched the seepage characteristics of a tunnel under the conditions of high ground stress and highwater pressure by model tests and found that the expansion of the original fractures caused by tunnel excavation eventually led to water inrush geohazards. Previous research has promoted the analysis of the mechanism of water inrush in tunnels and provided important guidance for the prevention and control of water inrush geohazards in tunnel construction. However, these studies primarily investigated a single geological structure, and relatively few studies investigated the mechanism and evolution process of water inrush in tunnels in geological environments where multiple geological structures coexist. Tunnel construction is gradually developing toward deep burial and super-long areas, and it is difficult to avoid water inrush geohazards

in complex geological environments. Therefore, it is of great practical significance and engineering value to clarify the mechanism and evolution process of water inrush in tunnels in geological environments where multiple geological structures coexist.

In this study, a water inrush geohazard in a deep-buried water-conveyance tunnel under the complex geological environment of the karst cave-fractured zone in China was selected as an engineering background. First, a large-scale physical three-dimensional (3D) model test under the aforementioned geological environment was performed. Multivariate physical information, such as the displacement, stress, and seepage pressure of the surrounding rock, was monitored during the model test. Via comprehensive comparative analysis, the sensitivity priority of precursor information of the tunnel water inrush was determined. Second, a conceptual model for the evolution process of water inrush geohazards was proposed based on the primary feature of the water inrush geohazard in the engineering background and that in the model test. Finally, based on fracture mechanics, a simplified theoretical model of water inrush geohazards was established, and the formulas describing the critical water pressure of water inrush geohazards under two failure models of tensile-shear fracture failure and compression-shear fracture failure were deduced. The results of this study can provide a useful reference for the construction design and risk prediction of water inrush in deep-buried tunnels under the complex geological environment of karst cave-fractured zones.

1 ENGINEERING BACKGROUND

A deep-buried water-conveyance tunnel in China is considered to provide background to this study. To solve the problem of ecological water consumption in the lower reaches of River A, the water from River E is transferred to River A. Magnetotelluric method, engineering geological mapping, and field geological survey were used to carry out special surveys of the water-conveyance tunnel. The deep-buried water-conveyance tunnel is 55.19 km (K0+000–K55+050), and the simplified geological map of it is shown in Fig. 1a. The exploration data showed that the strata traversed by the tunnel were mainly Triassic conglomerate, limestone, and tuff, and the tunnel had to pass through four fault zones, namely F1, F2, F3, and F4. The conglomerate is gray-white with a fractured structure, the main components are mudstone, limestone, calcareous cementation. Limestone is gray-white, moderately weathered, and fine-crystalline structure. The tuff is light gray with a tuff structure and a massive structure. The debris is mainly quartz, feldspar, and dark minerals. The glass debris content is about 10%–30%. The tunnel was constructed by the mining method and divided into two benches. The height of the upper bench and the lower bench were 2 and 4 m, respectively. The tunnel was excavated in order from the upper bench to the lower bench. After the upper bench was excavated for 10 m, the lower bench started to be excavated. The tunnel was supported by anchoring and shotcreting, and a few 500 cm long grouted hollow bolts were applied to support the surrounding rock in the tunnel vault. The primary support was C25 shotcrete and the thickness was 25 cm, which inside was reinforced by steel fabric.

The middle section of the tunnel (see the red block diagram in Fig. 1a) is the key control project. The total length and the maximum buried depth were 13.7 km and 720 m respectively. The annual precipitation is 1 583 mm. Groundwater was primarily affected by rainwater, and the water pressure varied from 0.1 to 2.5 MPa over one year according to the geological investigation report. When the tunnel was excavated to the section of K23+616, a water inrush geohazard occurred before the primary support due to the influence of sudden heavy rain on the surface, as shown in Fig. 1b. The comprehensive geophysical exploration map of the water inrush geohazard area was shown in Fig. 2. The section of K23+580–K23+860 (see the blue block diagram in Fig. 2) is the intersection of the karst development area and the F2 fault. The F2 fault intersected the tunnel at the right angle with a dipping angle of 78° . The apparent resistivity was 150 to 600 $\Omega \cdot \text{m}$, and it was inferred that the rock mass was moderately weathered. Under the influence of the F2 fault, the rock mass was in a broken state. Karst pipelines or dissolution fissures were developed, which were connected with surface karst depressions and caves, and the rock mass was rich in water.

The tunnel section of K23+600–K23+640 (see the red block diagram in Fig. 2) was selected as the prototype and the comprehensive research flow diagram as shown in Fig. 3. The diameter and burial depth of the tunnel in the study area are approximately 6 and 700 m, respectively. Based on the comprehensive geophysical exploration map and the structure of the tunnel exposed after the water inrush geohazard, there was an irregular spherical karst cave located above the tunnel, and its width was approximately 6.1 m by manual measurement. The bottom of the karst cave was approximately 5.9 m away from the tunnel vault. And a large number of interlaced structural planes derived from the F2 fault led to the development of a fractured zone that extended long and vertically cut through a karst cave as a result of geological transformation and groundwater erosion. The width of the fractured zone was approxi-

mately 0.1–0.5 m. The karst cave and fractured zone provided a suitable geological environment for water inrush. According to China's surrounding rock classification system presented in the code for engineering geological investigation of water resources and hydropower, the rock masses are classified as Grade IV.

2 INDOOR MODEL TEST

The evolution of water inrush in the deep-buried tunnel under the abovementioned complex geological environment was reproduced through model tests. The change laws of the multivariate information, such as displacement, stress, and seepage pressure of surrounding rock, were also analyzed.

2.1 Model Test Design

2.1.1 Model test system and material

The model test system independently designed by Shandong University (China) was used in the model test (Yang et al., 2019), as shown in Fig. 4a. The maximum load that can be exerted on each surface is 3 000 kN, and the loading pressure can be held for 720 h. A tunnel portal was engineered in the center of the back-loading plate for the excavation of the tunnel, as shown in Fig. 4b. The length, width, and height of the box mold are 1 500, 1 000, and 1 000 mm, respectively, as shown in Fig. 4c.

The tunnel section of K23+600–K23+640 in the tunnel was selected as the engineering prototype of the model test, and the surrounding rock mass was considered Grade IV. The diameter and burial depth of the tunnel were set equal to 6 and 700 m, respectively. Considering the abovementioned factors, the geometry ratio (C_L) was set equal to 50, and the reduced density scale (C_ρ) was 1. The similarity relationship of the physical model test was determined based on the physical equations, equilibrium equations, geometric equations, fluid-solid coupling theory, and boundary conditions, as shown in Table 1. The modeled material is composed of chlorinated paraffin,

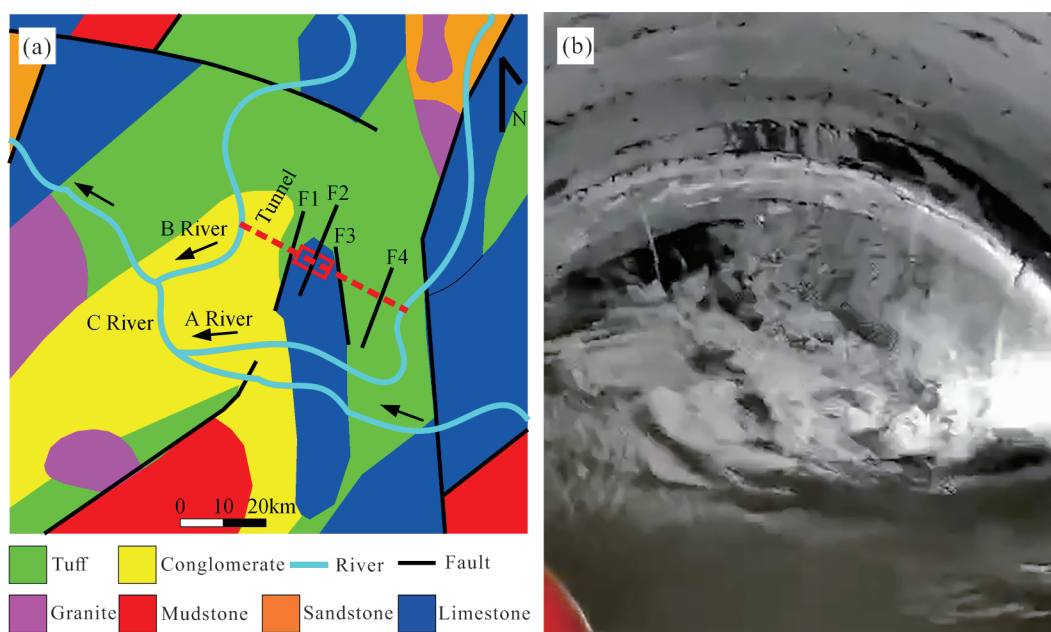


Figure 1. Simplified geological map and water inrush geohazard. (a) Simplified geological map of the tunnel; (b) water inrush geohazard.

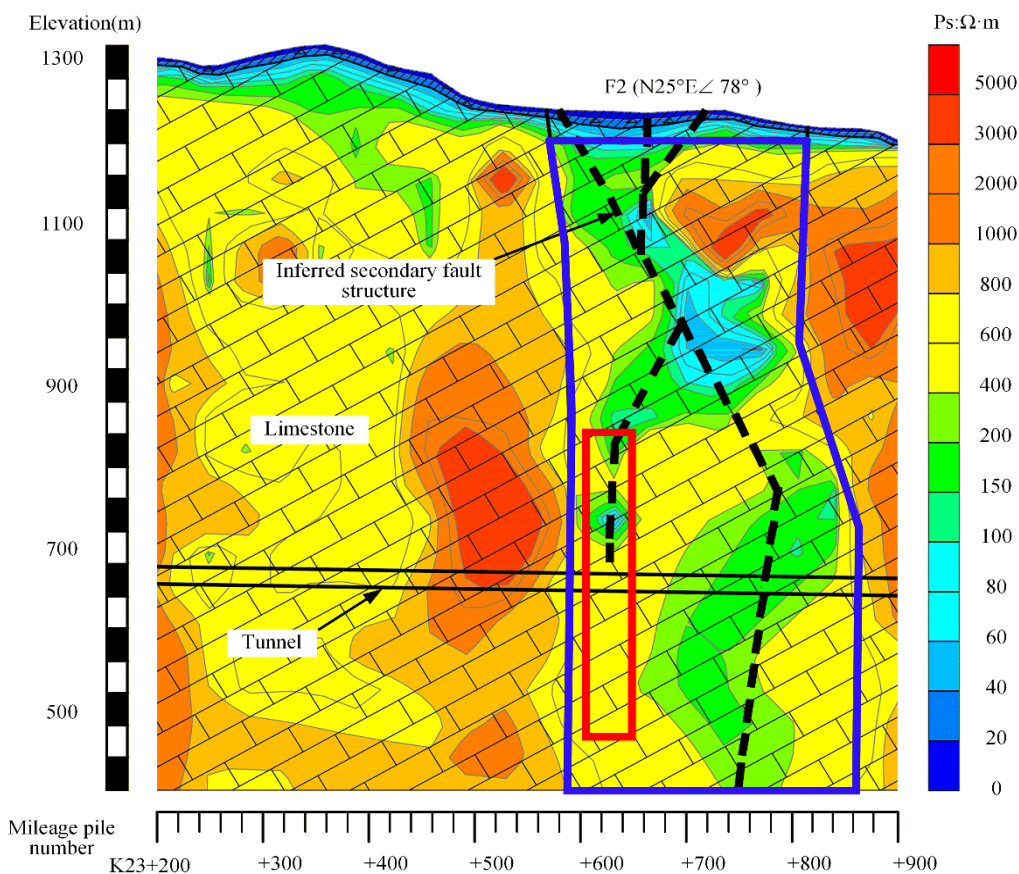


Figure 2. Comprehensive geophysical exploration map of the study area.

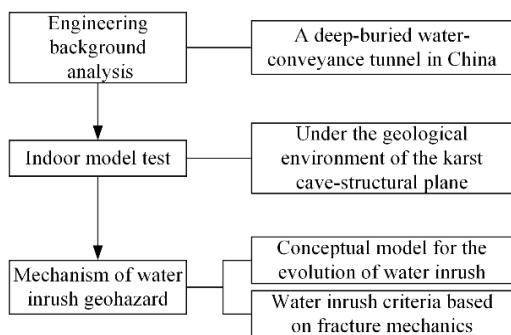


Figure 3. The comprehensive research flow diagram.

white cement, iron powder, calcium carbonate, silicone oil, and standard sand. The mass ratio of the modeled material that meets the requirements of the model test is 1 : 0.34 : 0.068 : 0.25 : 0.075 : 0.103, and water is also used. The physical and mechanical parameters of the original rock and similar materials are shown in Table 2.

2.1.2 Model test design

The internal structural characteristics of the model test are shown in Fig. 5a. Karst cave A was located directly above the central axis of the tunnel and connected to an inlet pipe, and its diameter was 120 mm. The distance between its bottom and the tunnel vault was 120 mm. Structural plane A was rectangular and bisected karst cave A vertically. The width and height of structural plane A were 360 and 480 mm, respectively, and

Table 1 The similarity relationship of the model test

Parameters	Relations	Reduced scale
Stress	$C_\sigma = C_L C_\gamma$	50
Strain	$C_\epsilon = C_\mu$	1
Elasticity modulus	$C_E = C_\sigma / C_\epsilon$	50
Poisson's ratio	$C_\mu = C_\epsilon$	1
Friction coefficient	$C_\phi = C_\mu$	1
Hydraulic conductivity	$C_K = \sqrt{C_L} / C_\gamma$	7.07
Cohesion	$C_c = C_\sigma$	50

Table 2 Physical and mechanical parameters of the original rock and model

Item	Surrounding rock	Modeling materials
Density (g·cm ⁻³)	2.40–2.72	2.47
Compressive strength (MPa)	10–40	0.67
Elasticity modulus (GPa)	3.0–5.0	0.08
Poisson's ratio	0.35	0.32
Cohesion (MPa)	1.5–2	0.028
Hydraulic conductivity (cm·s ⁻¹)	9.18×10 ⁻⁶ –3.14×10 ⁻⁵	3.19×10 ⁻⁶
Friction angle (°)	31–36	33

its upper boundary was 60 mm from the top of karst cave A. The central axis of the tunnel was perpendicular to structural plane A. The lower boundary of structural plane A was 60 mm from the bottom of the tunnel, and its left and right boundaries were 180 mm from the central axis of the tunnel. Two monitoring sections were used in the model test and were denoted as I-1 and I-2, as shown in Fig. 5b. I-L is a vertical displacement monitoring line in the waterproof rock mass. The monitoring elements buried in the model test were primarily miniature soil pressure gauges, miniature osmometers, strain bricks, and displacement gauges, as shown in Fig. 6.

2.2 Model Construction and Procedures

2.2.1 Model construction

It is difficult to prefabricate karst caves filled with confined water in model tests. A new method for making karst caves was proposed by taking advantage of ice-melt properties in this paper. The primary production process is shown in Fig. 7. In this study, a new device was also designed to make the karst cave-structural plane, and the primary components of the device are shown in Fig. 8.

According to the internal structure of the model detailed in Section 2.1, the experimental sample was divided into four



Figure 4. The true triaxial physical model test system. (a) The model test apparatus; (b) back-loading plate; (c) the box mold.

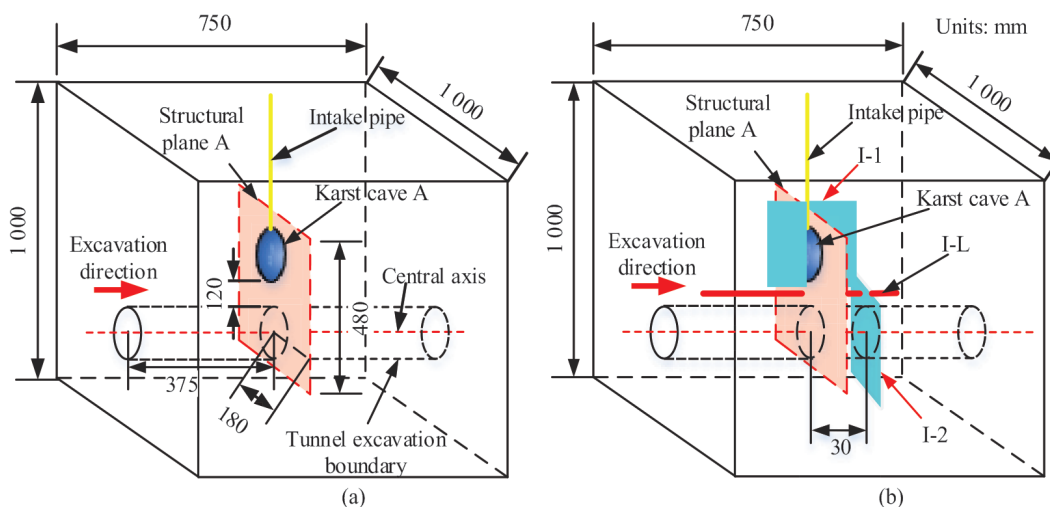


Figure 5. Schematic diagram of the model. (a) Overall diagram of the model; (b) model monitoring scheme.

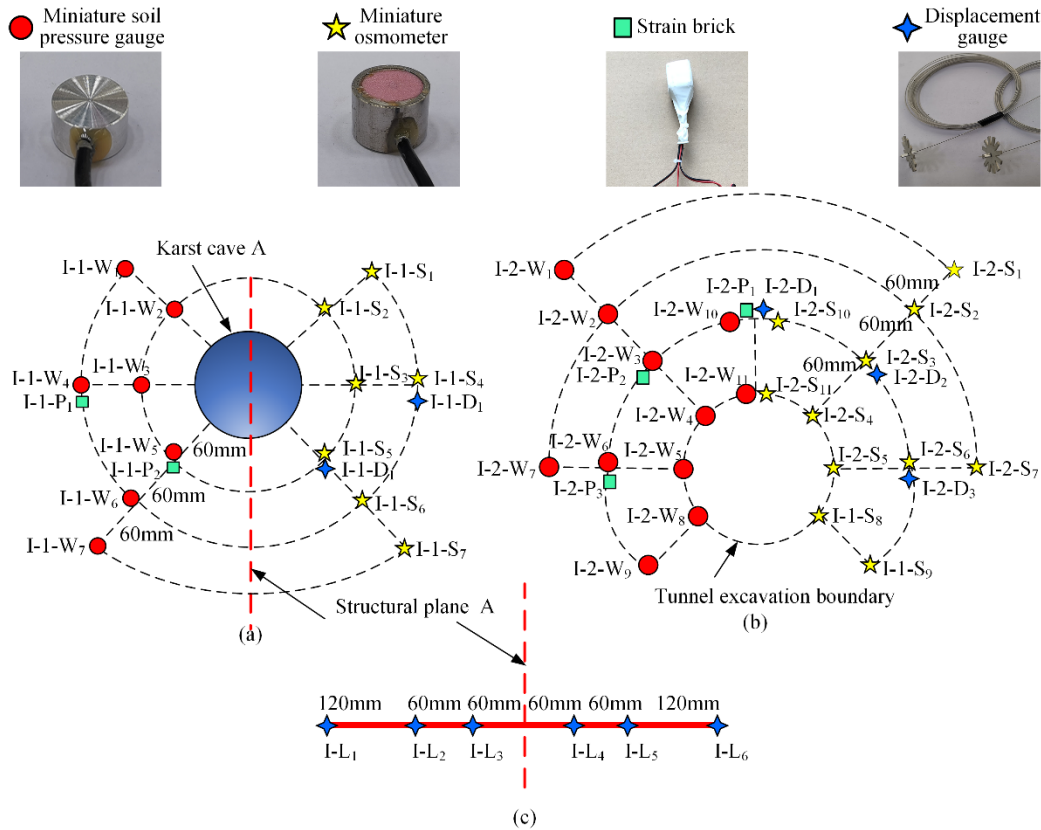


Figure 6. Model monitoring scheme. (a) Monitoring section I-1; (b) M = monitoring section I-2; (c) vertical displacement monitoring line I-L.

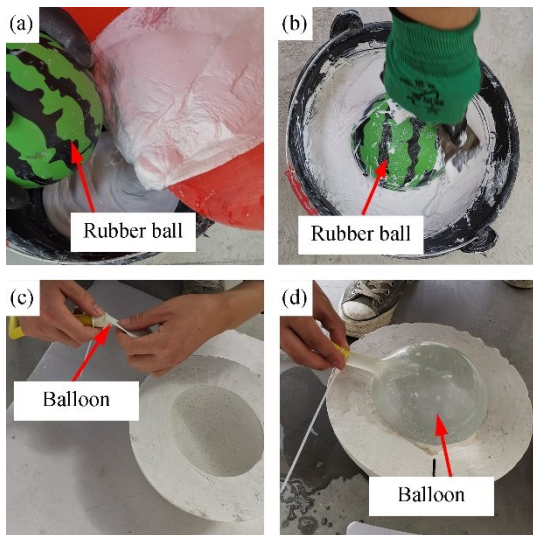


Figure 7. The production of the ice ball. (a) Pouring the gypsum slurry; (b) repairing of the cavity; (c) placing the balloon; (d) balloon filled with water.

parts from bottom to top in the construction. The heights of the four parts were 370, 240, 240, and 150 mm. The construction of the karst cave-structural plane was considered to be an example to introduce the model body filling, and the processes are shown as follows:

(1) The position of the structural plane was marked on the top of part II, and the wooden box and plank were put into the box mold, as shown in Fig. 9a.

(2) Silicone oil was sprayed evenly on the top of part II,

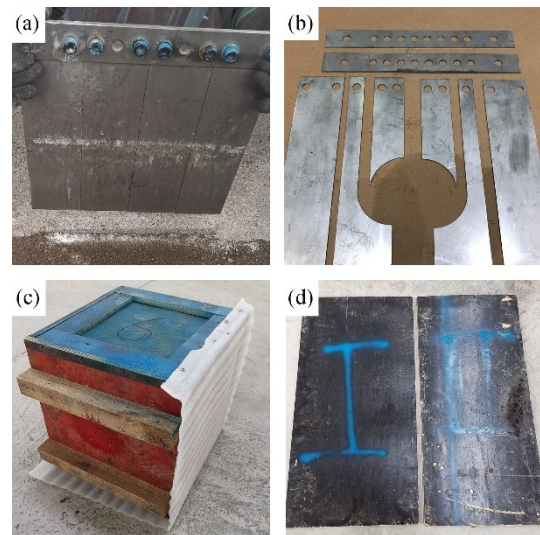


Figure 8. Device for making the karst cave-structural plane. (a) Common composite steel plate; (b) composite steel plate with a circular hole; (c) wooden box; (d) plank.

as shown in Fig. 9b. Then, the ready-mixed similar materials were added to the box mold and initially rammed into place, as shown in Fig. 9c. The same method was used to fill the rest of the mold after the wooden boxes were removed.

(3) The locations of the karst cave and structural plane are marked and slotted, as shown in Fig. 9d.

(4) The iceball prefabricated in the previous section was embedded into the composite steel plate with a circular hole.

Then, the steel plate and the iceball were placed into the gap after the plank was pulled out, as shown in Fig. 9e.

(5) Silicone oil was evenly sprayed into the gap, as shown in Fig. 9f. Similar materials were quickly backfilled and compacted at the end of this step.

(6) The steel plate was dismantled, and its components were removed in sequence, as shown in Fig. 9g. A certain amount of mica powder filled the gap, as shown in Fig. 9h.

(7) Similar materials in the position where the intake pipe would be installed were excavated, and then an intake pipe was put into position, as shown in Fig. 9i. Finally, similar materials were backfilled and compacted.

(9) The embedding of monitoring elements is shown in Fig. 10. The spatial locations and corresponding monitoring elements of the monitoring points were determined based on the monitoring scheme detailed in Section 2.1.2.

2.2.2 Model procedures

The real buried depth of the tunnel was 700 m, which was

equivalent to a simulated buried depth of 14 m. According to the real buried depth and the similarity ratio, the vertical stress provided by the vertical stress loading system was 320 kPa. The ratio of horizontal stress to vertical stress was set equal to 0.4. According to the design of the model test, the excavation length was 750 mm. The testing process included tunnel excavation and karst cave hydraulic pressure loading.

The entire testing process is summarized as follows. (1) The horizontal and vertical pressures of the model were loaded to 136 and 320 kPa in 8 steps, and the interval of each step was 2 h. (2) The intake valve of karst cave A was opened, and its initial water pressure was loaded into 5 kPa. (3) The tunnel was excavated in 15 steps, and the length of each excavation was 50 mm, which was equivalent to 2.5 m at the project site. (4) After the excavation of the tunnel reached 750 mm, the water pressure of karst cave A was increased step by step with a gradient of 5 kPa every 0.25 h. When water inrush occurred, increasing the hydraulic pressure was stopped.

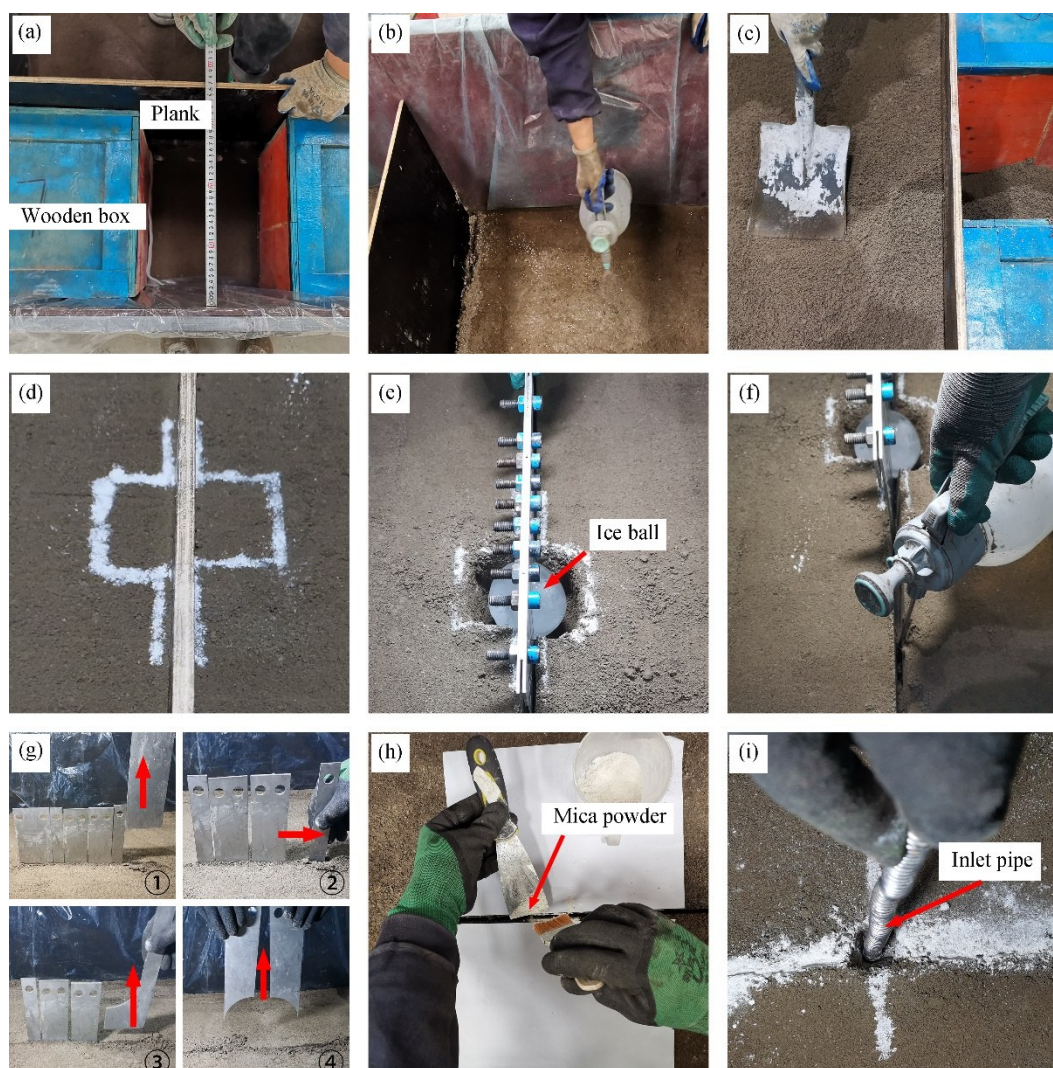


Figure 9. The fabrication of karst cave-structural plane. (a) Positioning of the structural plane; (b) spraying of silicone oil; (c) material compaction; (d) position of the karst cave slotted; (e) device embedding; (f) spraying of silicone oil; (g) removal of device; (h) mica powder filling; (i) inlet pipe laying.

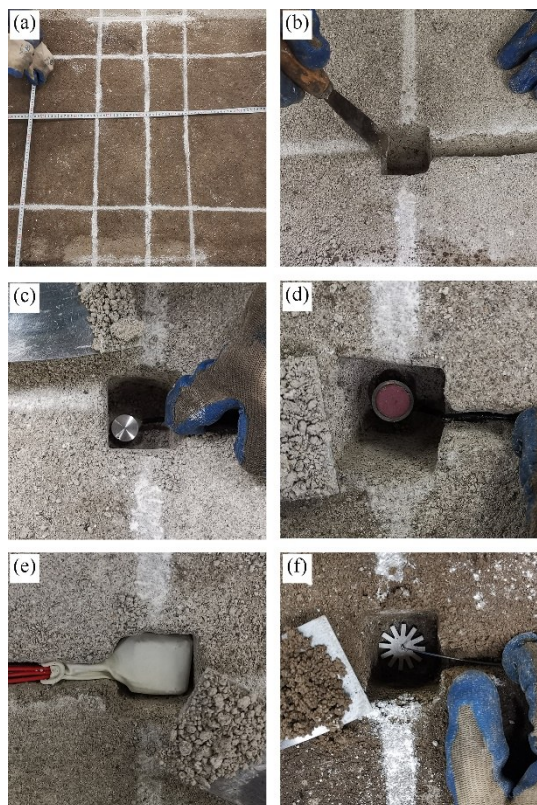


Figure 10. Embedding of monitoring elements. (a) Positioning of monitoring elements; (b) excavation of the positioning point; (c) miniature soil pressure gauge; (d) miniature osmometer; (e) strain brick; (f) displacement gauge.

2.2.3 Phenomenon of water inrush

Water inrush geohazards primarily occurred in the stage of hydraulic pressure loading. Thus, this section only describes the phenomenon that appears in that stage.

In the initial stage of karst cave hydraulic pressure loading, water droplets gradually appeared on the vault of the tunnel with the loading of the hydraulic pressure, as shown in Fig. 11a. With the continuous increase in hydraulic pressure, the seepage velocity at the vault of the tunnel was accelerated, and the flow pattern changed from a point-like drip to a line-like drip, as shown in Fig. 11b. This result indicated that the surrounding rock cracks were expanding continuously. When the hydraulic pressure of the karst cave increased to 40 kPa, a few rocks started to detach from the vault of the tunnel and gradually spread to the arch shoulder of the tunnel, and eventually, water inrush occurred in the arch shoulder of the tunnel, as shown in Figs. 11c, 11d.

2.3 Result and Analysis

According to the characteristics of the water inrush in the engineering background, three monitoring points (I-2-D₁, I-2-W₁₀, and I-2-S₁₀) in the waterproof rock mass were emphatically analyzed and were all in monitoring Section I-2.

2.3.1 Comprehensive comparison during the tunnel excavation

Figure 12 shows the variation curves of vertical displace-

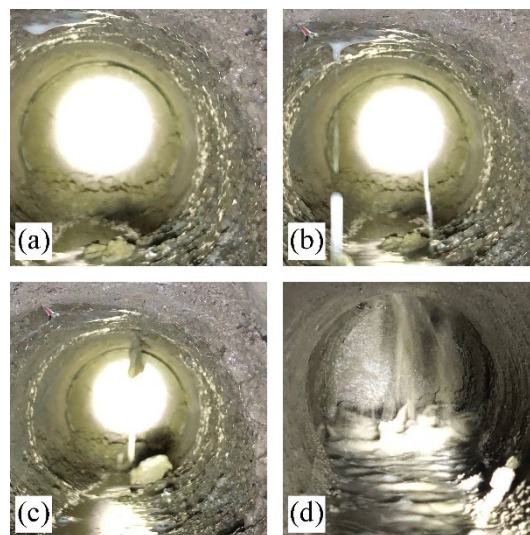


Figure 11. The process of water inrush in the model test. (a) Water droplets; (b) line-like drip water; (c) rock mass falling; (d) water inrush.

ment, vertical stress, and seepage pressure corresponding to I-2-D₁, I-2-W₁₀, and I-2-S₁₀ during tunnel excavation. With the tunnel excavated, the vertical displacement gradually increased, while the vertical stress and seepage pressure gradually decreased. The entire process of vertical displacement can be divided into the initial steady stage, the slow increasing stage, the markedly increasing stage, and the final steady stage four stages. Also, that of the vertical stress and seepage pressure can be divided into the initial steady stage, the slow decreasing stage, the markedly decreasing stage, and the final steady stage.

The vertical displacement of I-2-D₁ and the vertical stress of I-2-W₁₀ began to change in step 3 of tunnel excavation when the tunnel face was approximately 300 mm from monitoring Section I-2. Also, the seepage pressure of I-2-S₁₀ began to change in step 4 when the tunnel face was approximately 250 mm from monitoring Section I-2. When step 9 was completed, the tunnel passed through structural plane *A* and monitoring Section I-2, the vertical displacement increased markedly from A_{1D} (displacement was 1.01 mm) to B_{1D} (displacement was 2.08 mm), and the sharp increase in vertical displacement was 1.08 mm. Concurrently, the vertical stress decreased markedly from A_{1W} (stress value was 339.13 kPa) to B_{1W} (stress value was 254.57 kPa), indicating a drop of 84.56 kPa. When step 10 was completed, the seepage pressure increased markedly from A_{1S} (seepage stress value was 2.99 kPa) to B_{1S} (stress value was 1.98 kPa), indicating an increase of 1.01 kPa. The vertical displacement and stress gradually stabilized after the completion of step 12 when the tunnel face was approximately 200 mm from monitoring Section I-2, while the seepage pressure remained stable after the completion of step 13 when the tunnel face was approximately 250 mm from monitoring Section I-2. The final stable values of vertical displacement, vertical stress, and seepage pressure were 3.236 mm, 239.11 kPa, and 1.71 kPa, respectively.

According to these analyses, the following conclusion can be obtained. (1) The change in seepage pressure showed a hysteresis phenomenon, and the vertical displacement and stress

were more sensitive to the disturbance of tunnel excavation. The vertical displacement and stress can be used as the key monitoring items for predicting water inrush geohazards in real projects under the geological environment of karst cave-fractured zones with low water pressure. The primary reason for the hysteresis of seepage pressure was that the hydraulic pressure of the underground water system was small and stable in the tunnel excavation stage, and the change in seepage pressure was primarily due to the expansion of the original cracks and the generation of new cracks caused by the tunnel excavation. Only when the change in displacement and stress accumulate to a certain extent can the expansion of original cracks and the generation of new cracks occur. (2) Jump points A_{ID} and A_{IW} occurred after the tunnel face crossed structural plane A and before monitoring Section I-2, which indicated that the excavation disturbance range of the karst cave-structural plane zone was larger than that of the ordinary surrounding rock mass. Therefore, the support strength of the karst cave-structural plane zone should be strengthened during tunnel construction.

2.3.2 Comprehensive comparison during karst cave hydraulic pressure loading

Variations in the vertical displacement, vertical stress, and seepage pressure of the aforementioned three points during karst cave hydraulic pressure loading are shown in Fig. 12. The variations in the vertical displacement and vertical stress were highly consistent with those described in Section 2.3.1. In the initial stage of karst cave hydraulic pressure loading, the seepage pressure increased with increasing hydraulic pressure in the karst cave, and when the seepage pressure reached its peak, it suddenly decreased, as shown in Fig. 13.

Figure 13 also shows that when the hydraulic pressure was loaded for 2 h when the hydraulic pressure of the karst cave was 40 kPa, the vertical displacement, vertical stress, and seepage pressure changed markedly and concurrently, which indicated that water inrush geohazards occurred in the tunnel.

The vertical displacement of I-2- D_1 jumped from the Z_{D1} point (displacement was 4.98 mm) to the Z_{D2} point (displacement was 6.49 mm), indicating a sharp increase in vertical displacement equal to 1.51 mm. The vertical stress of I-2- W_{10} dropped markedly from Z_{W1} (stress value was 150.07 kPa) to Z_{W2} (stress was 114.61 kPa), indicating a sharp release of stress equal to 35.46 kPa. The seepage pressure curve of I-2- S_{10} decreased markedly from Z_{S1} (seepage pressure was 25.03 kPa) to Z_{S2} (seepage pressure was 10.30 kPa), indicating an instantaneous release of seepage pressure equal to 14.73 kPa.

Thus, with increasing hydraulic pressure in the karst cave, the hydraulic pressure began to play a leading role in the destruction of the tunnel. The vertical displacement, vertical stress, and seepage pressure showed abrupt changes concurrently when water inrush geohazards occurred in the tunnel, and the hysteresis phenomenon of the seepage pressure was weakened. The suddenness of water inrush geohazards in the tunnel was also more marked. In addition, comparing the stage of tunnel excavation and karst cave hydraulic pressure loading in the model test, the changes in vertical displacement, vertical stress, and seepage pressure in the former were found to be bigger than the latter; thus, the total energy released in the stage of karst cave hydraulic pressure loading was more than the stage of the tunnel excavation, resulting in the expansion of original cracks and the generation of new cracks that were fully developed and connected in the stage of hydraulic pressure loading.

3 MECHANISM OF WATER INRUSH GEOHAZARD

3.1 Conceptual Model for the Evolution of Water Inrush

The disturbance caused by tunnel excavation will destroy the equilibrium state of the groundwater system in surrounding rock and induce the expansion and penetration of original cracks, and the generation of new cracks, leading to water inrush geohazards in the tunnel (Wang et al., 2021; Zhang et al., 2017; Moon and Fernandez, 2010; Carranza-Torres and Fairhurst, 2000). Groundwater is an important factor that af-

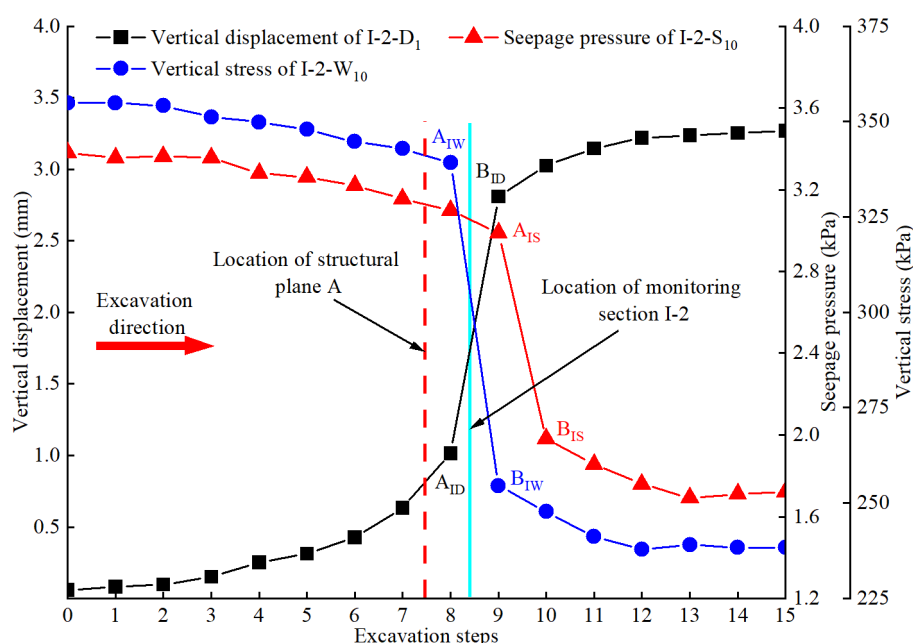


Figure 12. Variation laws of vertical displacement, vertical stress, and seepage pressure during the tunnel excavation.

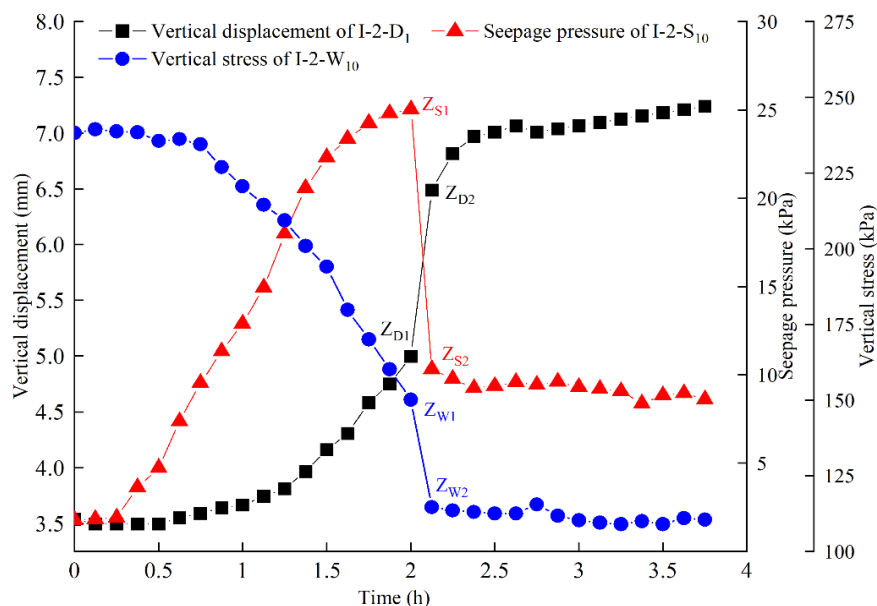


Figure 13. Variation laws of vertical displacement, vertical stress, and seepage pressure in the hydraulic pressure loading process.

ffects the evolution process of water inrush geohazards in tunnels. When the groundwater system has poor connectivity with the surface, the water pressure in the surrounding rock is relatively constant, and the water inrush geohazard is controlled by the fracture instability of the rock mass (Nodintsev and Amilenko, 2015). When the groundwater system is well linked to the ground surface, rainwater can flow into it, increasing the groundwater pressure and reducing the strength of the rock body. Water inrush geohazards occur in the tunnel under the combined action of rainwater and excavation disturbance (Lan et al., 2021; Xu et al., 2021; Su et al., 2020; Wu et al., 2020; Zhou et al., 2020; Lin et al., 2019).

According to the description in Section 1 (engineering background), the primary feature of the water inrush geohazard was that the water inrush geohazard didn't occur in the tunnel section of K23+616 until there was heavy rain on the surface. Based on the aforementioned characteristics and the phenomenon of water inrush in the model test, a conceptual model for the evolution process of water inrush geohazards was proposed and divided into the following four stages.

(1) The stage of the initial balance: because the tunnel face was far away from the karst cave-fractured zone, the excavation disturbance had little influence on the karst cave-fractured zone, and the groundwater system and ground stress were both in equilibrium, as shown in Fig. 14a.

(2) The propagation of original cracks: with the advancement of the tunnel face, the karst cave-fractured zone was gradually affected by tunnel excavation, and the surrounding rocks located on both sides of it began to show large uneven settlements. These uneven settlements caused the original cracks to expand and eventually form a structural plane, as shown in Fig. 14b. The entire process was accompanied by the creation of a few new cracks.

(3) The formation of the dominant water inrush channel: during the rainy season, rainfall increases and flows into the groundwater system through the karst cave, fractured zone, and

structural plane, which leads to the structural plane extending in the direction of the tunnel. Concurrently, new cracks keep increasing, and dominant water inrush channels begin to appear in the waterproof rock mass, as water leakage gradually occurs on the vault of the tunnel, as shown in Fig. 14c, which agreed with the phenomenon of Fig. 11a. However, due to the low connectivity rate of newly formed cracks, the waterproof rock mass can still block water.

(4) The instability of the waterproof rock mass: with increasing rainfall, the water pressure in the groundwater system gradually increases. When the water pressure in the structural plane is greater than its normal stress, the structural plane begins to open and gradually extends to the tunnel. Then, new cracks become fully developed and connected. Under the joint action of the structural plane and new cracks, the waterproof rock mass becomes cut into a large number of weakly connected or isolated rock masses. When the connection between the rock mass and the surrounding rock is not sufficient to support the vertical stress and water pressure, the rock mass fails and becomes unstable. Then, the failure rock mass and water flow into the tunnel, and the tunnel exhibits water inrush, as shown in Fig. 14d. This stage primarily corresponds to the third and fourth stages of the model test proposed in Section 2.2.3.

3.2 Water Inrush Criteria Based on Fracture Mechanics

3.2.1 Theoretical model

The mechanism of water inrush geohazards in the deep-buried tunnel under the complex geological environment of the karst cave-fractured zone was analyzed based on fracture mechanics. Based on the comprehensive geophysical exploration map (Fig. 2) and the structure of the tunnel exposed after the water inrush geohazard, the shape of the karst cave was irregular spherical and the width of the fractured zone was approximately 0.1–0.5 m, so the shape of the karst cave was simplified as spherical and the fractured zone was simplified as a structural plane in the theoretical model. Because the results of the

model test indicated that the excavation disturbance range of the karst cave-structural plane zone was larger than that of the ordinary surrounding rock mass, this paper assumed the most unfavorable situation in which some original cracks in the karst cave-fractured zone expanded to form a structural plane under the influence of tunnel excavation, and the structural plane penetrated both the karst cave and the tunnel.

The structural plane intersected the karst cave and tunnel at points A and B, respectively, and the distance between points was L , as shown in Fig. 15b. The vertical and horizontal stresses in the far-field of the structural plane were σ_H and σ_V , respectively. The angle between the structural plane and σ_H is α . The water pressure acting on the structural plane was considered to be the karst cave water pressure P , and it is assumed that the water pressure acted equally in all directions of the structural plane. The stress state of the structural plane can be expressed as (1)

$$\begin{cases} \sigma_\alpha = -\left(\frac{\sigma_H + \sigma_V}{2} - \frac{\sigma_H - \sigma_V}{2} \cos 2\alpha - P\right) \\ \tau_\alpha = -\left|\frac{\sigma_H - \sigma_V}{2} \sin 2\alpha\right| \end{cases} \quad (1)$$

When the stress generated by σ_H and σ_V in the normal direction of the structural plane is less than the cave hydraulic pressure P , σ_α is the tensile stress, and when it is greater than the karst water pressure P , σ_α is the compressive stress. Therefore, the failure mode of the tunnel was divided into compression-shear fracture failure and tensile-shear fracture failure based on the fracture mechanics.

Considering the ratio of σ_V and σ_H to be equal to λ , the expression of λ is easily described by

$$\lambda = \frac{\sigma_V}{\sigma_H} \quad (2)$$

3.2.2 Tensile-shear fracture failure

When σ_α is a tensile stress, the failure model of the tunnel is tensile-shear fracture failure and is described by the problem of I-II tensile-shear composite cracks. Approximate fracture judgment criteria in engineering were selected to facilitate engineering applications, and the crack propagation criterion can be expressed as

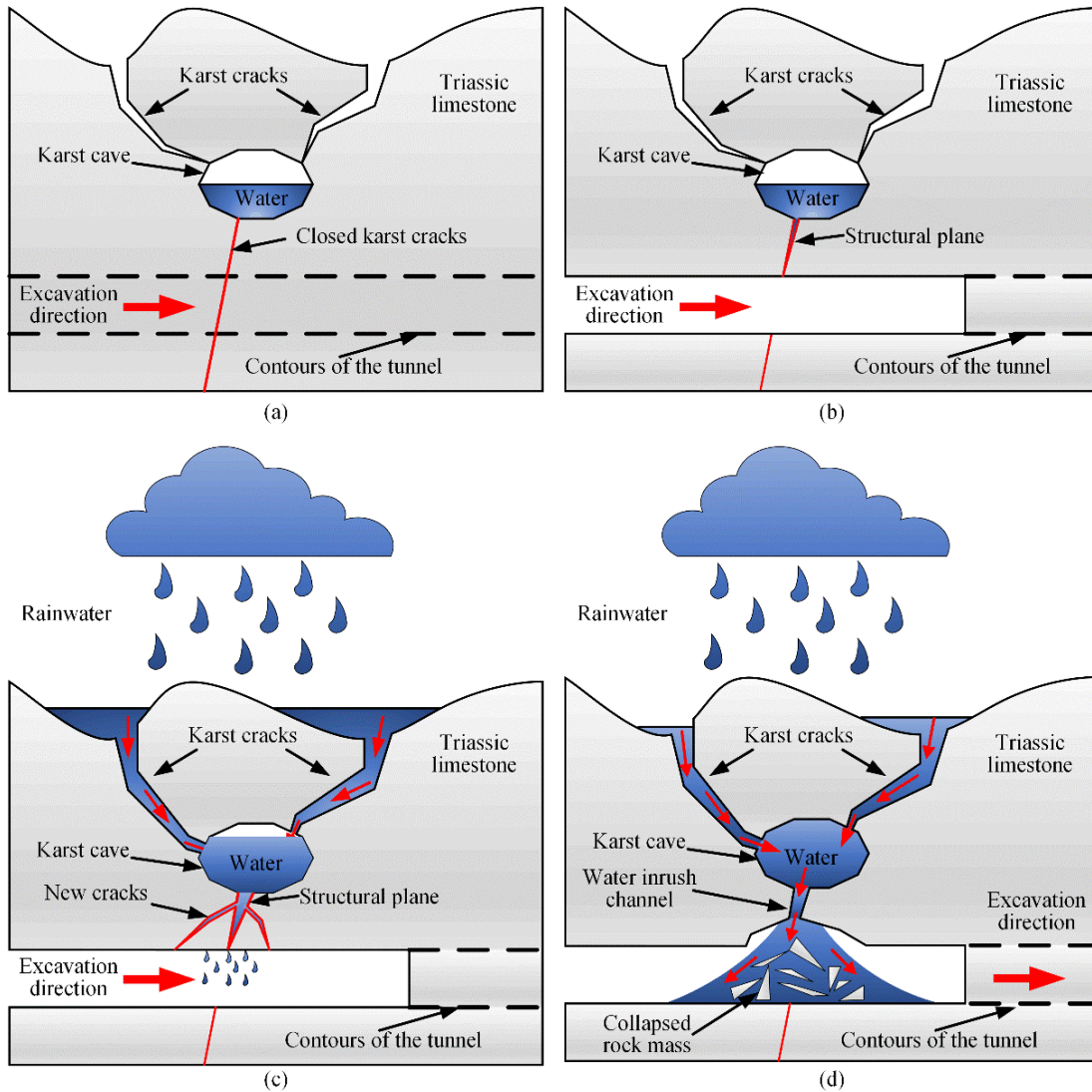


Figure 14. The conceptual model for the evolution process of water inrush. (a) The stage of the initial balance; (b) the propagation of original cracks; (c) the formation of the dominant water inrush channel; (d) the instability of the waterproof rock mass.

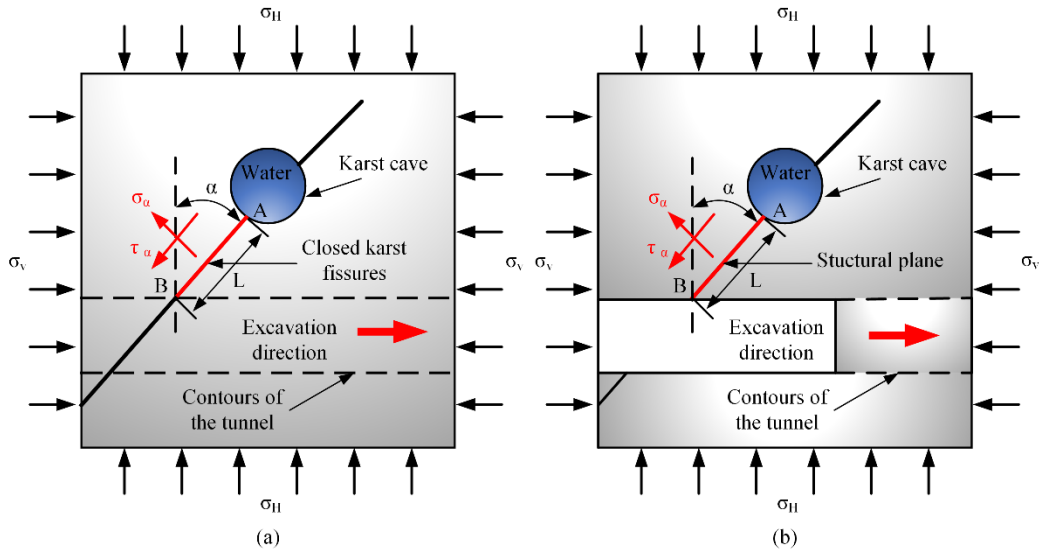


Figure 15. Mechanical model of surrounding rock with a structural plane. (a) Before tunnel excavation; (b) after tunnel excavation.

$$K_I + K_{II} = K_{IC} \quad (3)$$

where K_{IC} is the mode I fracture toughness value, and K_I and K_{II} are the mode-I and -II stress intensity factors, respectively.

Based on fracture mechanics, K_I and K_{II} can be expressed as

$$K_I = \sigma_a \sqrt{\pi a} \quad (4)$$

$$K_{II} = \tau_a \sqrt{\pi a} \quad (5)$$

where a is the length of the semicrack, which is considered to be L .

According to Eqs. (1)–(5), the critical water pressure P_t under the failure model of tensile-shear fracture failure is described by

$$P_t = \frac{\lambda + 1}{2} \sigma_H + \frac{\lambda - 1}{2} \sigma_H \cos 2\alpha + \left| \frac{\lambda - 1}{2} \sigma_H \sin 2\alpha \right| + \frac{K_{IC}}{\sqrt{\pi L}} \quad (6)$$

To analyze the variation of P_t with λ , P_{λ} is defined as

$$P_{\lambda} = \frac{P_t - \frac{K_{IC}}{\sqrt{\pi L}}}{\sigma_H} \quad (7)$$

Substituting Eq. (6) into Eq. (7), P_{λ} can be described by

$$P_{\lambda} = \frac{1 + \lambda}{2} + \frac{\lambda - 1}{2} \cos 2\alpha + \left| \frac{\lambda - 1}{2} \sin 2\alpha \right| \quad (8)$$

Based on Eq. (8), the relationship between P_{λ} and α can be obtained, as shown in Fig. 16. The following conclusions can be drawn from Fig. 16. (1) When λ remains constant, P_{λ} is symmetric about the plane $\alpha = 90^\circ$, and in the range of $\alpha = 0^\circ - 90^\circ$, as α increases, P_{λ} first increases and then decreases. (2) When $\lambda < 1$, the minimum value of P_{λ} appears at $\alpha = 0^\circ$, which shows that the tunnel is most prone to water inrush geohazards when the structural plane is in the vertical direction. (3) When $\lambda = 1$, P_{λ} does not change with α . (4) When $\lambda > 1$, the minimum value of P_{λ} appears at $\alpha = 90^\circ$, which means that the tunnel is most vulnerable to water inrush geohazards when the structural plane is

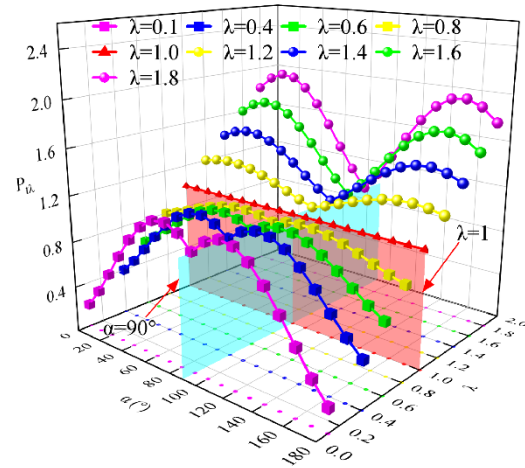


Figure 16. Relationship between P_{λ} and α under tension-shear mixed cracking.

in the horizontal direction.

3.2.3 Compression-shear fracture failure

When σ_a is a compressive stress, the failure model of the tunnel is compression-shear fracture failure, which is described by the problem of II compression-shear cracks. The crack propagation criterion can be described by

$$K_{II} = K_{IIc} \quad (9)$$

where K_{IIc} is the mode-II fracture toughness.

The closed crack can transfer normal stress and shear stress after contact, and the effective shear stress on the crack surface is

$$\tau_e = \tau_a - (\sigma_a \tan \varphi + c) \quad (10)$$

where φ is the friction angle of the structural plane, φ is 30° in this study, and c is the cohesion of the structural plane, which is 0 in this study.

The mode-II stress intensity factor is calculated by the effective shear stress on the crack surface

$$K_{II} = \tau_e \sqrt{\pi a} \quad (11)$$

From Eqs. (1), (2), (9), (10), and (11), the critical water pressure P_c under the failure model of compression-shear fracture failure can be described by

$$P_c = \frac{\lambda + 1}{2} \sigma_H + \frac{\lambda - 1}{2} \sigma_H \cos 2\alpha - \frac{1}{\tan \varphi} \left[\left| \frac{\lambda - 1}{2} \sigma_H \sin 2\alpha \right| + \frac{K_{IIc}}{\sqrt{\pi L}} \right] \quad (12)$$

To analyze the variation of P_c with λ , P_{ci} is defined as

$$P_{ci} = \frac{P_c + \frac{1}{\tan \varphi} \frac{K_{IIc}}{\sqrt{\pi L}}}{\sigma_H} \quad (13)$$

Substituting Eq. (12) into Eq. (13), P_{ci} can be described by

$$P_{ci} = \frac{1 + \lambda}{2} + \frac{\lambda - 1}{2} \cos 2\alpha - \frac{1}{\tan \varphi} \left| \frac{\lambda - 1}{2} \sin 2\alpha \right| \quad (14)$$

From Formula (14), P_{ci} as a function of α was obtained, as shown in Fig. 17, which leads to the following conclusions. (1) When λ remains constant, P_{ci} is symmetric about plane $\alpha = 90^\circ$, and in the scope of $\alpha = 0^\circ - 90^\circ$, P_{ci} first decreases and then increases with the increase of α . (2) When $\lambda < 1$, the minimum value of P_{ci} occurs at $\alpha = 30^\circ$, indicating that the tunnel is most vulnerable to water inrush at this time. (3) When $\lambda = 1$, P_{ci} does not change with α . (4) When $\lambda > 1$, the minimum value of P_{ci} occurs at $\alpha = 90^\circ$, which means that the tunnel is most prone to water inrush disasters.

4 VERIFICATION OF WATER INRUSH CRITERION

According to the description in Section 2.2.2, in the engineering prototype of the model test, the vertical and horizontal ground stresses were 17 and 6.8 MPa, respectively; the length of the semicrack L was 6 m; And the friction angle of the crack surface φ was 30° . Based on the results reported by Huang et al. (2020) $K_{IC} = 15.2 \text{ MN/m}^{3/2}$ and $K_{IIc} = 11.2 \text{ MN/m}^{3/2}$ (Guo and Qiao, 2012; Gan, et al., 2007; Huang, et al., 2000). Substituting these parameters into Formulas (6) and (12), the critical hydraulic pressures of the water inrush geohazard under the two failure models of tensile-shear fracture failure and compression-shear fracture failure were determined to be 10.30 and 2.33 MPa, respectively.

Section 2.3.2 shows that when the hydraulic pressure of the karst cave was loaded to approximately 40 kPa in the model test, water inrush geohazards occurred in the tunnel, which indicated that the critical water pressure of the water inrush geohazard in the engineering prototype of the model test was approximately 2 MPa based on the similarity relationship in Table 1.

By comparing the results of theoretical calculations and model tests, the calculated critical hydraulic pressure (2.33 MPa) was found to be similar to the measured critical hydraulic inrush pressure (approximately 2 MPa), which validated the correctness of the theoretical model and calculation formulae. In the model test, the failure model of the tunnel was compression-shear fracture failure.

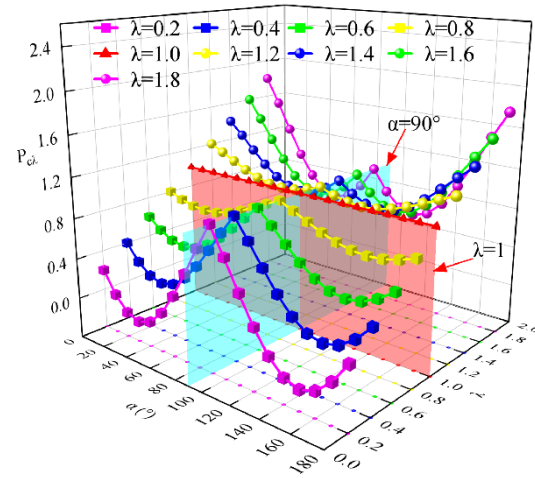


Figure 17. Relationship between P_{ci} and α under compression-shear mixed cracking.

5 CONCLUSIONS

The mechanism and evolution of the water inrush geohazard in the complex geological environment within a karst cave-fractured zone were investigated by model testing and theoretical analysis. The primary conclusions of this study are summarized below.

(1) A new method and devices for making the geological environment, where the karst cave and the structural plane co-exist, were proposed, which informs a new way for the construction of the co-existence of multiple geological structures in the model test.

(2) The expansion of original cracks and the generation of new cracks were primarily caused by tunnel excavation during the stage of tunnel excavation in the model test. The change in seepage pressure exhibited hysteresis, and the vertical displacement and stress were more sensitive to the disturbance of tunnel excavation. Therefore, the vertical displacement and stress can be used as the key monitoring items to predict water inrush geohazards in actual projects under the geological environment of karst cave-fractured zones with low hydraulic pressure.

(3) With increasing hydraulic pressure in the karst cave, hydraulic pressure began playing a leading role in the destruction of the tunnel, resulting in the hysteresis phenomenon of the seepage pressure being weakened, and the suddenness of water inrush geohazards in the tunnel was more marked.

(4) A conceptual model for the evolution process of water inrush geohazards in the deep-buried tunnel under the aforementioned geological environment was built based on the characteristics of the water inrush geohazard in the engineering background and that in the model test. The evolution of water inrush geohazards can be divided into four stages: the stage of the initial balance, the propagation of original cracks, the formation of the dominant water inrush channel, and the instability of the waterproof rock mass.

(5) A simplified theoretical model of water inrush geohazards was developed. Based on the theoretical model, the calculation formulas for the critical hydraulic pressure of the water inrush geohazard under two failure models of tensile-shear fracture failure and compression-shear fracture failure were de-

duced. The calculated critical hydraulic pressure was similar to the measured critical hydraulic pressure in the model test, which validated the accuracies of the theoretical model and associated formulae. And the failure model of water inrush geohazards is compression-shear fracture failure.

ACKNOWLEDGMENTS

This work was supported by the National Natural Science Foundation of China (Nos. 41731284, 41920104007). The final publication is available at Springer via <https://doi.org/10.1007/s12583-022-1619-z>.

REFERENCES CITED

- Ameguid, M. A., Saada, O., Nunes, M. A., et al., 2008. Physical Modeling of Tunnels in Soft Ground: A Review. *Tunnelling and Underground Space Technology*, 23(2): 185–198. <https://doi.org/10.1016/j.tust.2007.02.003>
- Carranza-Torres, C., Fairhurst, C., 2000. Application of the Convergence-Confinement Method of Tunnel Design to Rock Masses that Satisfy the Hoek-Brown Failure Criterion. *Tunnelling and Underground Space Technology*, 15(2): 187–213. [https://doi.org/10.1016/s0886-7798\(00\)00046-8](https://doi.org/10.1016/s0886-7798(00)00046-8)
- Farhadian, H., Katibeh, H., Huggenberger, P., 2016. Empirical Model for Estimating Groundwater Flow into Tunnel in Discontinuous Rock Masses. *Environmental Earth Sciences*, 75(6): 1–16. <https://doi.org/10.1007/s12665-016-5332-z>
- Fu, H. L., An, P. T., Cheng, G. W., et al., 2021. Calculation of the Safety Thickness of Water Inrush with Tunnel Axis Orthogonal to Fault. *Arabian Journal of Geosciences*, 14(11): 1–11. <https://doi.org/10.1007/s12517-021-07297-8>
- Gan, K. R., Yang, Y., Li, J. S., 2007. Analysis on Karst Water Inflow Mechanisms and Determination of Thickness of Safe Rock Walls: Case Study on a Tunnel. *Tunnel Construction*, 3: 13–16 (in Chinese with English Abstract)
- Guo, J. Q., Qiao, C. S., 2012. Study on Water-Inrush Mechanism and Safe Thickness of Rock Wall of Karst Tunnel Face. *Journal of the China Railway Society*, 34(3): 105–111 (in Chinese with English Abstract)
- Hu, H., Zhang, B. W., Zuo, Y. Y., et al., 2018. The Mechanism and Numerical Simulation Analysis of Water Bursting in Filling Karst Tunnel. *Geotechnical and Geological Engineering*, 36(2): 1197–1205. <https://doi.org/10.1007/s10706-017-0386-6>
- Huang, R. Q., Wang, X. N., Chen, L. S., 2000. Hydro-Splitting off Analysis on Underground Water in Deep-Lying Tunnels and Its Effect on Water Gushing out. *Chinese Journal of Rock Mechanics and Engineering*, 19(5): 573–576 (in Chinese with English Abstract)
- Huang, Z., Zeng, W., Wu, Y., et al., 2019. Experimental Investigation of Fracture Propagation and Inrush Characteristics in Tunnel Construction. *Natural Hazards*, 97(1): 193–210. <https://doi.org/10.1007/s11069-019-03634-z>
- Jiang, H. M., Li, L., Rong, X. L., et al., 2017. Model Test to Investigate Waterproof-Resistant Slab Minimum Safety Thickness for Water Inrush Geohazards. *Tunnelling and Underground Space Technology*, 62: 35–42. <https://doi.org/10.1016/j.tust.2016.11.004>
- Lan, X. D., Zhang, X., Yin, Z. C., et al., 2021. Mitigation of Karst Tunnel Water Inrush during Operation in Seasonal Variation Zone: Case Study in Nanshibi Tunnel. *Journal of Performance of Constructed Facilities*, 35(3): 04021010. [https://doi.org/10.1061/\(asce\)cf.1943-5509.0001573](https://doi.org/10.1061/(asce)cf.1943-5509.0001573)
- Li, L. P., Tu, W. F., Shi, S. S., et al., 2016. Mechanism of Water Inrush in Tunnel Construction in Karst Area. *Geomatics, Natural Hazards and Risk*, 7(S1.): 35–46. <https://doi.org/10.1080/19475705.2016.1181342>
- Li, S. C., Liu, H. L., Li, L. P., et al., 2016. Large Scale Three-Dimensional Seepage Analysis Model Test and Numerical Simulation Research on Undersea Tunnel. *Applied Ocean Research*, 59: 510–520. <https://doi.org/10.1016/j.apor.2016.07.013>
- Li, S. C., Xu, Z. H., Huang, X., et al., 2018. Classification, Geological Identification, Hazard Mode and Typical Case Studies of Hazard-Causing Structures for Water and Mud Inrush in Tunnels. *Chinese Journal of Rock Mechanics and Engineering*, 37(5): 1041–1069 (in Chinese with English Abstract)
- Li, S. C., Lin, P., Xu, Z. H., et al., 2015. Minimum Safety Thickness of Water and Mud Inrush Induced by Filled-Type Karst Water Bearing Structures Based on Theory of Slice Method. *Rock and Soil Mechanics*, 36(7): 1989–1994 (in Chinese with English Abstract)
- Liang, D. X., Jiang, Z. Q., Zhu, S. Y., et al., 2016. Experimental Research on Water Inrush in Tunnel Construction. *Natural Hazards*, 81(1): 467–480. <https://doi.org/10.1007/s11069-015-2090-2>
- Lin, P., Li, S. C., Xu, Z. H., et al., 2019. Water Inflow Prediction during Heavy Rain while Tunneling through Karst Fissured Zones. *International Journal of Geomechanics*, 19(8): 04019093. [https://doi.org/10.1061/\(asce\)gm.1943-5622.0001478](https://doi.org/10.1061/(asce)gm.1943-5622.0001478)
- Liu, J. Q., Chen, W. Z., Nie, W., et al., 2019. Experimental Research on the Mass Transfer and Flow Properties of Water Inrush in Completely Weathered Granite under Different Particle Size Distributions. *Rock Mechanics and Rock Engineering*, 52(7): 2141–2153. <https://doi.org/10.1007/s00603-018-1719-3>
- Moon, J., Fernandez, G., 2010. Effect of Excavation-Induced Groundwater Level Drawdown on Tunnel Inflow in a Jointed Rock Mass. *Engineering Geology*, 110(3/4): 33–42. <https://doi.org/10.1016/j.enggeo.2009.09.002>
- Nodintsev, V. N., Miletenko, N. A., 2015. Water Inrush in Mines as a Consequence of Spontaneous Hydrofracture. *Journal of Mining Science*, 51(3): 423–434. <https://doi.org/10.1134/s1062739115030011>
- Pan, D. D., Li, S. C., Xu, Z. H., et al., 2019. Experimental and Numerical Study of the Water Inrush Mechanisms of Underground Tunnels Due to the Proximity of a Water-Filled Karst Cavern. *Bulletin of Engineering Geology and the Environment*, 78(8): 6207–6219. <https://doi.org/10.1007/s10064-019-01491-5>
- Park, K. H., Owatsiriwong, A., Lee, J. G., 2008. Analytical Solution for Steady-State Groundwater Inflow into a Drained Circular Tunnel in a Semi-Infinite Aquifer: A Revisit. *Tunnelling and Underground Space Technology*, 23(2): 206–209. <https://doi.org/10.1016/j.tust.2007.02.004>
- Paul, W., 2008. The Role of the Epikarst in Karst and Cave Hydrogeology: A Review. *International Journal of Speleology*, 37(1): 1–10
- Simpson, B., Tatsuoka, F., 2008. Geotechnics: The Next 60 Years. *Géotechnique*, 58(5): 357–368. <https://doi.org/10.1680/geot.2008.58.5.357>
- Su, H. J., Feng, Y. J., Guo, Q. Z., et al., 2020. Model Experimental Study on the Seepage and Failure Features of Tunnel under Wetting-Drying Alternation with Increasing Water Pressure. *Geofluids*, 2020: 1–11. <https://doi.org/10.1155/2020/8845528>
- Sun, J., Wang, S. J., 2000. Rock Mechanics and Rock Engineering in China: Developments and Current State-of-the-Art. *International Journal of Rock Mechanics and Mining Sciences*, 37(3): 447–465. [https://doi.org/10.1016/s1365-1609\(99\)00072-6](https://doi.org/10.1016/s1365-1609(99)00072-6)
- Wang, H. F., Wang, M. Y., 2013. Infiltration Experiments in Layered Structures of Upper Porous and Lower Fractured Media. *Journal of Earth Science*, 24(5): 843–853. <https://doi.org/10.1007/s12583-013-0378-2>

- Wang, X. L., Lai, J. X., Qiu, J. L., et al., 2020. Geohazards, Reflection and Challenges in Mountain Tunnel Construction of China: A Data Collection from 2002 to 2018. *Geomatics, Natural Hazards and Risk*, 11(1): 766–785. <https://doi.org/10.1080/19475705.2020.1747554>
- Wang, Y. C., Li, Z. Y., Jing, H. W., et al., 2021. Study on the Seepage Characteristics of Deep Buried Tunnels under Variable High-Pressure Water Heads. *Bulletin of Engineering Geology and the Environment*, 80(2): 1477–1487. <https://doi.org/10.1007/s10064-020-01986-6>
- Wu, J., Li, S. C., Xu, Z. H., et al., 2019. Determination of Required Rock Thickness to Resist Water and Mud Inrush from Karst Caves under Earthquake Action. *Tunnelling and Underground Space Technology*, 85: 43–55. <https://doi.org/10.1016/j.tust.2018.11.048>
- Wu, T. Y., Jia, J. H., Jiang, N., et al., 2020. Model Test of Deformation Evolution and Multi Factor Prediction of Anchorage Slope Stability under Rainfall Condition. *Journal of Earth Science*, 31(6): 1109–1120. <https://doi.org/10.1007/s12583-020-1343-5>
- Xu, Z. H., Lin, P., Xing, H. L., et al., 2021. Hydro-Mechanical Coupling Response Behaviors in Tunnel Subjected to a Water-Filled Karst Cave. *Rock Mechanics and Rock Engineering*, 54(8): 3737–3756. <https://doi.org/10.1007/s00603-021-02423-0>
- Xue, Y. G., Kong, F. M., Qiu, D. H., et al., 2021. The Classifications of Water and Mud/Rock Inrush Hazard: A Review and Update. *Bulletin of Engineering Geology and the Environment*, 80(3): 1907–1925. <https://doi.org/10.1007/s10064-020-02012-5>
- Yang, W. M., Wang, M. X., Zhou, Z. Q., et al., 2019. A True Triaxial Geomechanical Model Test Apparatus for Studying the Precursory Information of Water Inrush from Impermeable Rock Mass Failure. *Tunnelling and Underground Space Technology*, 93: 103078. <https://doi.org/10.1016/j.tust.2019.103078>
- Yang, X. L., Xiao, H. B., 2016. Safety Thickness Analysis of Tunnel Floor in Karst Region Based on Catastrophe Theory. *Journal of Central South University*, 23(9): 2364–2372. <https://doi.org/10.1007/s11771-016-3295-6>
- Zhang, G. H., Jiao, Y. Y., Wang, H., et al., 2017. On the Mechanism of Inrush Hazards when Denghuozhai Tunnel Passing through Granite Contact Zone. *Tunnelling and Underground Space Technology*, 68: 174–186. <https://doi.org/10.1016/j.tust.2017.05.008>
- Zhang, L. W., Fu, H., Wu, J., et al., 2021. Effects of Karst Cave Shape on the Stability and Minimum Safety Thickness of Tunnel Surrounding Rock. *International Journal of Geomechanics*, 21(9): 04021150. [https://doi.org/10.1061/\(asce\)gm.1943-5622.0002054](https://doi.org/10.1061/(asce)gm.1943-5622.0002054)
- Zhang, Q., Wang, J., Feng, L. F., 2021. Mechanical Mechanism of Hydraulic Fracturing Effect Caused by Water Inrush in Tunnel Excavation by Blasting. *Mathematical Problems in Engineering*, 2021: 9919260. <https://doi.org/10.1155/2021/9919260>
- Zhao, Y. L., Zhang, L. Y., 2018. Experimental Study on the Mud-Water Inrush Characteristics through Rock Fractures. *Advances in Civil Engineering*, 2018: 2060974. <https://doi.org/10.1155/2018/2060974>
- Zhou, Z., Zhang, J. M., Ning, F. L., et al., 2020. Large-Scale Test Model of the Progressive Deformation and Failure of Cracked Soil Slopes. *Journal of Earth Science*, 31(6): 1097–1108. <https://doi.org/10.1007/s12583-020-1342-6>
- Zhu, J. Q., Li, T. Z., 2020. Catastrophe Theory-Based Risk Evaluation Model for Water and Mud Inrush and Its Application in Karst Tunnels. *Journal of Central South University*, 27(5): 1587–1598. <https://doi.org/10.1007/s11771-020-4392-0>